



**HAL**  
open science

## Thermo-mechanical simulations of laser heating experiments on UO<sub>2</sub>

Matthieu Reymond, Jerome Sercombe, Laurent Gallais, Thomas Doualle,  
Yves Pontillon

► **To cite this version:**

Matthieu Reymond, Jerome Sercombe, Laurent Gallais, Thomas Doualle, Yves Pontillon. Thermo-mechanical simulations of laser heating experiments on UO<sub>2</sub>. Journal of Nuclear Materials, 2021, 557, pp.153220. 10.1016/j.jnucmat.2021.153220 . hal-03466237

**HAL Id: hal-03466237**

**<https://hal.science/hal-03466237>**

Submitted on 25 Feb 2022

**HAL** is a multi-disciplinary open access archive for the deposit and dissemination of scientific research documents, whether they are published or not. The documents may come from teaching and research institutions in France or abroad, or from public or private research centers.

L'archive ouverte pluridisciplinaire **HAL**, est destinée au dépôt et à la diffusion de documents scientifiques de niveau recherche, publiés ou non, émanant des établissements d'enseignement et de recherche français ou étrangers, des laboratoires publics ou privés.



Distributed under a Creative Commons Attribution - NonCommercial - NoDerivatives 4.0 International License

# Thermo-mechanical simulations of laser heating experiments on $\text{UO}_2$

Matthieu Reymond<sup>a,b</sup>, Jérôme Sercombe<sup>a</sup>, Laurent Gallais<sup>b</sup>, Yves Pontillon<sup>a</sup>

<sup>a</sup>CEA, DEN, F-13108 Saint-Paul-lez-Durance, France

<sup>b</sup>Aix Marseille Univ, CNRS, Centrale Marseille, Institut Fresnel, Marseille, France

---

## Abstract

In this paper, a thermo-mechanical model suitable for the interpretation of laser heating experiments simulating the power increasing phase of a RIA transient is detailed. The thermal model includes a description of the heat deposition on the sample surface and of the heat transfer within the thickness and radius of the  $\text{UO}_2$  sample. The mechanical modeling describes cracking and crushing of the material depending on the loading mode (tension or compression dominated) and on temperature. The brittle - ductile transition in compression is in particular well reproduced. The parameters fitting is based on available uniaxial compression tests performed at high strain rates and on bending tests performed at moderate strain rates. The application of the mechanical model to the annular laser heating experiments led to a good estimation of the crushing and cracking location (near the sample periphery), of the crack orientation (circumferential) and of the beginning of cracking.

*Keywords:* Nuclear fuel modeling, Damage mechanics, Laser heating, Reactivity Initiated Accident

---

## 1. Introduction

2 Modeling of nuclear fuel in off normal conditions such as Reactivity Ini-  
3 tiated Accident (RIA) or Loss Of Coolant Accident (LOCA) is necessary  
4 to predict the response of the fuel under such extremes solicitations. Sim-  
5 ulations of RIA transients are worldwide performed by dedicated fuel per-  
6 formance codes such as ALCYONE at CEA [1, 2, 3] and others including  
7 SCANAIR [4, 5], FRAPTRAN [6], RANNS [7], FALCON [8]. Mostly ded-  
8 icated to the description of irradiated fuel rod thermomechanics, RIA fuel

9 performance code validation relies on experimental data coming from inte-  
10 gral experiments (i.e., on fuel rodlets) performed in research reactors such  
11 as CABRI [9] in France or the NSRR in Japan [10]. In spite of the gener-  
12 ally good reproduction of experimental trends by the fuel performance codes,  
13 some mechanisms remain difficult to tackle and require more research activ-  
14 ity. As pointed out in the recently published synthesis report on RIA [11],  
15 this is in particular the case of fission gas release during RIA which is mostly  
16 dependent on burnup and pulse characteristics (maximum power, width).  
17 The mechanism by which fission gas release proceeds during fast power tran-  
18 sients is thought to be grain boundary cracking related to fission gas bubbles  
19 overpressurization.

20 While providing crucial information, integral experiments on fuel rods  
21 cannot be used to perform parametric studies on one phenomenon since they  
22 are complex and costly. At CEA, to reproduce RIA transient thermal con-  
23 ditions, a laser-heating technique usable in a hot-cell environment is under  
24 development [12]. One of the main outcome expected from these experiments  
25 is to obtain valuable data regarding the mechanical behavior of nuclear fuel  
26 under the specific loading conditions taking place during a RIA (i.e., high  
27 temperatures and strain rates) with a focus on the mechanics behind the frag-  
28 mentation and grain boundary cracking of the fuel and fission gas release,  
29 especially in the restructured region of the pellet (High Burnup Structure).  
30 The impact of various parameters such as irradiation damage or fission prod-  
31 ucts on the phenomenology of fission gas release could be investigated in the  
32 future. Indeed, it is not clear from past integral experiments if the kinetics  
33 of fission gas release during a RIA transient is one of the driving parameters  
34 that can lead to rod failure. As such, it is important to propose complemen-  
35 tary experiments on irradiated fuel that can be multiplied for parametric  
36 studies.

37 In view of the objective of the laser heating experiments, numerical sim-  
38 ulation must be developed at the same time. It should furthermore not be  
39 limited to the thermal behavior of the fuel but should also include a precise  
40 description of the mechanical behavior of the fuel since it will be of primary  
41 importance for the identification of fission gas release mechanisms. In a first  
42 step towards this objective, this paper presents the development and vali-  
43 dation of a mechanical behavior law for non irradiated  $\text{UO}_2$ . Laser-heating  
44 experiments are used to investigate the relation between fuel fragmentation  
45 (grain boundary and macroscopic cracking) and thermomechanical loading  
46 representative of RIA conditions. A sophisticated material model is thus

47 proposed to describe micro- and macro-cracking of  $\text{UO}_2$  fuel both in tension  
48 and compression within a large range of temperatures. After a presentation  
49 of the laser heating experiments and of the material model, the simulation  
50 results are discussed and compared to on-line measurements.

## 51 2. Laser heating experiments

52 A Reactivity Initiated Accident thermal transient is characterized by the  
53 fast rise of power and of temperature that occurs in the fuel. In irradiated  
54 fuels, the increase of power and temperature can be strongly localized at the  
55 periphery of the pellet. Typical temperature increase obtained in research  
56 reactors are around 12273-1773 K (1000-1500°C) at the fuel pellet centerline  
57 and up to 2273 K (2000°C) at the pellet periphery, as shown in Figure 1.  
58 The temperature increase is quasi-adiabatic and happens in a few tens of  
59 milliseconds.

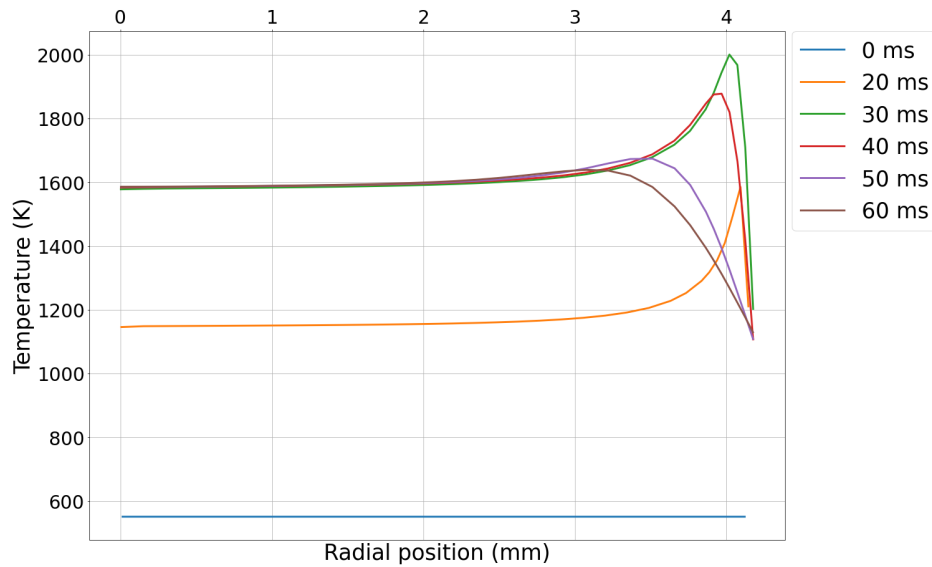


Figure 1: Radial temperature distribution calculated with ALCYONE fuel performance code during the NSRR RH-2 test (adapted from [1])

60 The capacity of laser-heating to reproduce RIA thermal transient at lab-  
61 oratory scale is based on the use of a high power Ytterbium fiber laser.  
62 Encouraging results have been reported in [12] with temperature as high as  
63 2273K (2000°C) being reached at the periphery of the sample in the few tens

64 of milliseconds.  $\text{UO}_2$  being a strongly absorbing material at the wavelength  
 65 used in the setup (1080 nm) [13, 14], laser power absorption is localized at  
 66 the surface of the samples. Accordingly, with a time scale of a few tens of  
 67 milliseconds, the sample thickness must be submillimetric if an homogenous  
 68 heating of the sample is expected. The samples are therefore prepared from  
 69 fuel pellets in the form of disks less than 1 mm thick.

70  
 71 The experiments presented in this paper are characterized by an annular  
 72 heating of the samples as shown in Figure 2.

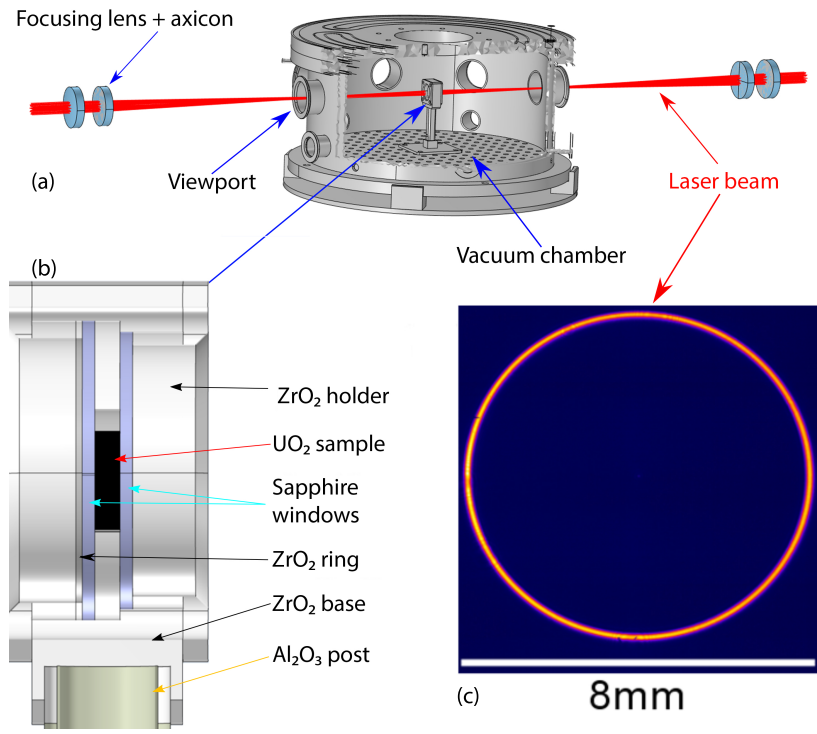


Figure 2: Sketch of the experimental chamber (a) and sample holder (b) used in the laser heating experiments. (c): Intensity profile of the laser beam obtained in the sample plane

73 The sample, which is obtained from  $\text{UO}_2$  fuel pellets fabricated at CEA  
 74 using a wet process followed by isostatic compaction at 450 MPa and sintering  
 75 at 1650°C during 2 h under flowing  $\text{H}_2$ , is placed vertically in a sample holder  
 76 made of zirconia with two optical sapphires that ensure optical access to the  
 77 sample and retain any possible fragments in case of loss of integrity. The disk,  
 78 sample holder and sapphires are placed in a dedicated experimental chamber

79 operated in vacuum ( $10^{-2}$  mbar) which allows monitoring and optical access  
80 through multiple viewports. The sample is first maintained at a starting  
81 temperature by a gaussian beam. It is then heated at its periphery by one  
82 or two annular gaussian beams of pre-selected dimensions (radius, waist).  
83 While not being strictly representative of a RIA, these experiments lead  
84 nevertheless to high strain rates and temperature increase rates that are of  
85 the order of magnitude of those encountered during fast power transients.

86 Two sets of experiments are presented in this paper. The first one is a  
87 series of 20 ms long laser heating experiments conducted on a  $970\ \mu\text{m}$  thick  
88 sample starting from a homogeneous temperature state of around  $800^\circ\text{C}$ . Dif-  
89 ferent powers are used, ranging from 150 to 1200 W with both faces of the  
90 sample being heated by two identical annular beams. The beam radius and  
91 waist are 3.5 and 0.5 mm, respectively. Real time temperature measurement  
92 by infrared imaging with a high speed thermal camera has been recorded  
93 during this series of experiments as showed on Figure 3 and will therefore be  
94 used to validate the thermal part of the simulations.

95 The second series consists of five heating experiments of duration ranging  
96 from 10 to 100 ms. The last one was performed with 300 W of laser power  
97 while the ones before used 150 W. These experiments were conducted on the  
98 same sample of thickness  $930\ \mu\text{m}$  and started from room temperature. Beam  
99 radius and waist are 3.9 and 0.1 mm, respectively. During these experi-  
100 ments, only one face of the sample is heated. Failure of the sample periphery  
101 happened brutally after around 40 ms of heating, as determined from the  
102 pictures taken with a high speed visible camera. The post experiment state  
103 of the sample is showed Figure 3.

104 The last two experiments of the second series (i.e., 100 ms - 150 W and  
105 100 ms - 300 W) will be used to validate the fuel mechanical behavior law  
106 presented in the next part.

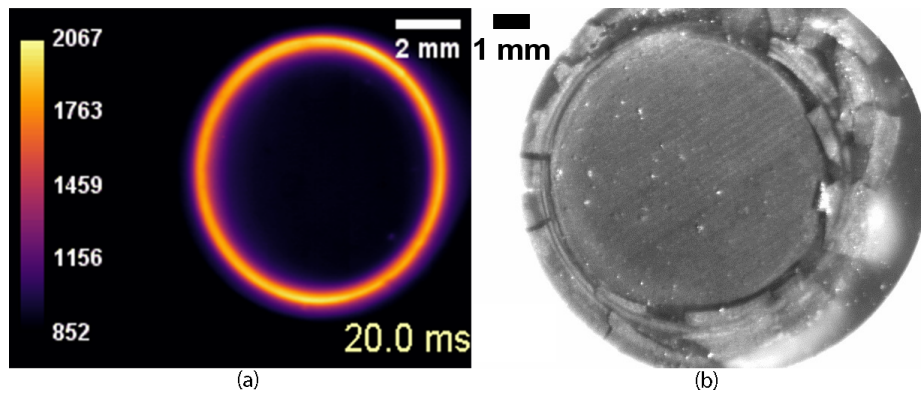


Figure 3: (a) False color image and corresponding temperature scale (in °C) obtained with the high speed infrared camera during the first series of experiments. Laser power was 900W and duration of the heating was 20ms. (b) Sample with a clear circumferential cracking of the periphery after the 100 ms - 300 W laser heating experiment of the second series of experiments

### 107 3. Mechanical behavior law for $\text{UO}_2$ submitted to laser heating

108 As most ceramics, uranium dioxide presents a brittle behavior at low and  
109 moderate temperature both in tension and compression. However, the frac-  
110 ture stress is dissymmetric: at room temperature, it can reach 1000 MPa in  
111 compression while it is around 100 MPa in tension. At higher temperatures,  
112 the behavior of  $\text{UO}_2$  becomes ductile. The brittle-ductile transition is not  
113 only dependent on temperature but also on the strain rate. In general, the  
114 higher the strain rate, the higher the temperature of transition from fragile  
115 to ductile behavior will be both for the compression domain [15, 16] and the  
116 tensile domain [17].

117 Salvo et al. obtained a brittle-ductile transition between 1100°C and  
118 1350°C at a strain rate of  $10^{-1}$ /s during uniaxial compression tests [15, 16].  
119 A ductile behavior with pronounced grain boundary cracking was observed  
120 at temperatures  $\geq 1550^\circ\text{C}$  leading compressive stresses close to 100 MPa.  
121 A brittle behavior with cracks parallel to the stress direction occurred at  
122 moderate temperature (1100°C).

123 Similar observations have been reported for the tensile domain by Evans  
124 et al. [18]. They identified a temperature of transition of around 1473 K  
125 (1200°C) from three points bending tests. Similarly, Canon et al. [17] found  
126 a temperature of transition of  $\sim 1473$  K (1200°C) from four points bending  
127 tests leading to an ultimate tensile stress of  $\sim 120$  MPa and to a strain rate  
128 of  $9.2/h$  ( $2 \cdot 10^{-3}$ /s). With strain rates usually exceeding 1/s during RIA  
129 transients, a brittle behavior is expected in tension even at high temperatures  
130 where the behavior would normally be ductile at lower strain rates.

131 To model the dissymmetric mechanical behavior of  $\text{UO}_2$  in tension and  
132 compression, the damage  $\mu$ -model proposed by Mazars et al. [19], classically  
133 used for concrete, is considered. It is an improved version of the first damage  
134 model developed by Mazars [20]. Damage is described by a scalar variable  
135  $d$  (evolution between 0 and 1) that is used to model the loss of stiffness  
136 of the material. Two distinct damage modes are considered for traction  
137 and compression, i.e. cracking and crushing, respectively. As such, both  
138 compressive and tensile loadings can lead to the development of damage  
139 and unilateral effects such as cracks opening and closure if the loading is  
140 reversed are considered in the model. Moreover, damage development is  
141 related to the first and second invariants of the strain tensor, meaning that  
142 the crack orientations are not fixed a priori in this model. This approach is  
143 more general than those used in many mechanical models available in fuel

144 performance codes [2], [21, 22] where the crack directions are prescribed by  
 145 the cylindrical coordinate system.

146 In the  $\mu$ -model the stress-strain relation is defined by:

$$\sigma = (1 - d) \mathbf{C} : \epsilon \quad (1)$$

147 with  $\sigma$  the standard Cauchy stress tensor,  $\mathbf{C}$  the elastic tensor and  $\epsilon$  the  
 148 elastic strain tensor.

149 To model damage, the equivalent strain concept is used. Cracking and  
 150 crushing are respectively associated to the following equivalent strains:

$$\epsilon_t = \frac{I_\epsilon}{2(1 - 2\mu)} + \frac{\sqrt{J_\epsilon}}{2(1 + \nu)} \quad (2)$$

151

$$\epsilon_c = \frac{I_\epsilon}{5(1 - 2\mu)} + \frac{6\sqrt{J_\epsilon}}{5(1 + \nu)} \quad (3)$$

152 with  $I_\epsilon$  and  $J_\epsilon$  as the first and second invariants of the elastic strain tensor  
 153 and  $\nu$  Poisson's ratio.

154 Two loading surfaces are then defined:

$$f_t = \epsilon_t - Y_t \quad \text{and} \quad f_c = \epsilon_c - Y_c \quad (4)$$

155 with  $Y_t$  and  $Y_c$  two thermodynamic variables related to the maximum  
 156 equivalent strains reached during the loading sequence:

$$Y_t = \text{Sup}[\epsilon_{0t}, \max(\epsilon_t)] \quad \text{and} \quad Y_c = \text{Sup}[\epsilon_{0c}, \max(\epsilon_c)] \quad (5)$$

157 Before damage onset,  $Y_t$  and  $Y_c$  are equal to the initial thresholds  $\epsilon_{0t}$  and  
 158  $\epsilon_{0c}$ . The effective damage  $d$  can then be estimated from the thermodynamic  
 159 variables  $Y_t$  and  $Y_c$  as follows:

$$d = -\frac{(1 - A)Y_0}{Y} - A \cdot \exp(B(Y - Y_0)) \quad (6)$$

160 with  $Y_0$  the initial value of  $Y$  defined by:

$$Y = rY_t + (1 - r)Y_c \quad (7)$$

161 and  $A$ ,  $B$  two parameters that are described by the following functions:

$$A = A_t(2r^2(1 - 2k) - r(1 - 4k)) + A_c(2r^2 - r + 1) \quad (8)$$

162

$$B = r^{(r^2-2r+2)}B_t + (1 - r^{(r^2-2r+2)})B_c \quad (9)$$

163 with  $r$  the triaxial factor indicating the nature of the stress.  $r = 0$  corre-  
 164 sponds to a uniaxial compression state and  $r = 1$  to a uniaxial tensile state.  
 165 When  $r = 1$ ,  $A = A_t$  and  $B = B_t$  and when  $r = 0$ ,  $A = A_c$  and  $B = B_c$ .  $k$   
 166 is a parameter that defines the asymptotic stress during pure shear loading,  
 167 see reference [19] for more details.

168 The four parameters  $A_t$ ,  $B_t$ ,  $A_c$  and  $B_c$  can be easily identified from strain-  
 169 stress curves obtained from uniaxial compression and tensile or bending tests.  
 170 Two strain thresholds activating the damage evolution need also to be defined  
 171 for tension and compression, i.e.,  $\epsilon_{t0}$  and  $\epsilon_{c0}$ , respectively.

172 The compression behavior of the model has been fitted on the strain-stress  
 173 curves of M. Salvo et al. [15, 16] obtained during uniaxial compression tests  
 174 at high strain rates ( $10^{-1}/s$ ) and high temperatures (1373-2023 K) represen-  
 175 tative of RIA loading conditions and which clearly led to a brittle-ductile  
 176 transition. The resulting model parameters are summarized in Table 1. The  
 177 extrapolation of the evolution of the parameters towards room temperature  
 178 is based on other existing uniaxial compressive tests [23, 24]. A decrease of  
 179 the compressive yield stress at temperatures higher than 1973 K (1700°C)  
 180 has been assumed with a target of 60 MPa around the melting temperature  
 181 of  $UO_2$  ( $\sim 3000$  K). The tensile behavior is assumed to remain brittle what-  
 182 ever the temperature reached and is characterized by a constant ultimate  
 183 tensile stress of around 80 MPa. Due to the lack of experimental data, the  
 184 asymptotic shear stress has been assumed null, leading to  $k = 1$ .

Parameter	Expression
$A_t$	3.2
$B_t$	2850
$\epsilon_{t0}$	0.00001
$A_c$	T < 1500 K: $A_c = 8.9719 \times 10^{-7} \times T^2 - 3.11509 \times 10^{-3} \times T + 2.8357$ T ≥ 1500 K: $A_c = 9.47303 \times 10^6 \times T^{-2.6154}$
$B_c$	T < 1500 K: $B_c = -0.828T + 173.59$ T ≥ 1500 K: $B_c = 50$
$\epsilon_{c0}$	T < 1500 K: $\epsilon_{c0} = -0.00001$ 1500 K ≤ T ≤ 2500 K: $\epsilon_{c0} = -4 \times 10^{-10} \times T^2 + 2 \times 10^{-6} \times T - 0.0032$ T > 2500K: $\epsilon_{c0} = -0.00058$
k	1

Table 1: Parameters of the  $\mu$ -model fitted to  $\text{UO}_2$

185 The model is solved numerically using the code generator Mfront [25]. A  
186 very interesting feature is the possible explicit integration of the stresses with  
187 the  $\mu$ -model. A large set of loading configurations (uniaxial, cyclic, biaxial,  
188 ...) and of temperatures, particularly around the temperature of transition,  
189 has been first tested with the mtest software (ensuring a calculation at a sin-  
190 gle material point) included in the MFront code generator. Figure 4 presents  
191 the stress-strain curves obtained for uniaxial tension and compression at con-  
192 stant temperatures varying between room temperature and 2773 K. As can  
193 be seen, the fragile-ductile temperature transition is set at 1500 K (1227°C).  
194 At temperatures below 1500 K, the compressive strain-strain curve is char-  
195 acterized by a decrease of the stress upon reaching a maximum value. The  
196 residual stress in each case is zero but it is reached at an increasing level  
197 of strain with the temperature increase. In Salvo’s et al. test performed at  
198 1373 K (1100°C) [16], the maximum stress was close to 300 MPa and soft-  
199 ening occurred till 15% of axial strain. At room temperature, the maximum  
200 stress in uniaxial compression is around -1000 MPa, consistent with the ex-

201 periments in the open literature [26]. At temperatures equal or above 1500  
 202 K, the behavior is characterized by a stress peak reached between 1 and 2%  
 203 of axial strain followed by a plateau at a stress level slightly lower than the  
 204 peak. This behavior is typical of  $\text{UO}_2$  tested at high temperature and has  
 205 been attributed to structural [24] or material [27] origin. In some of Salvo's  
 206 tests at high temperatures, the axial strain reached 20% without any sign of  
 207 softening. The tensile behavior is represented by a single stress-strain curve  
 208 since no temperature dependency has been considered in this work. The  
 209 maximum stress reaches 80 MPa and is followed by a fast decrease of the  
 210 stress leading a zero-stress value at an axial strain of 0.1%. For the behavior  
 211 of the  $\mu$ -model during biaxial loading conditions (compression-compression,  
 212 compression-tension or tension-tension) and the unilateral aspects (stiffness  
 213 recovery when compression loading follows tensile loading, i.e., cracks closure),  
 214 the interested reader may refer to the original paper of Mazars et al.  
 215 [19].

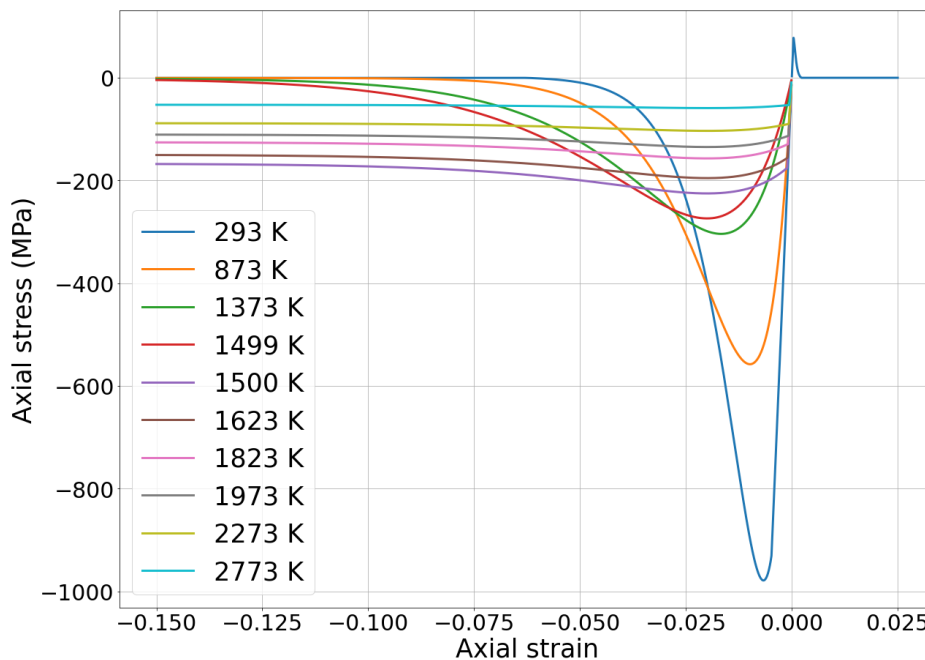


Figure 4: Stress-strain curves evolution with temperature as obtained from the  $\mu$ -model. The traction behavior is independent of temperature.

216 One important aspect of the proposed mechanical model for  $\text{UO}_2$  is the  
 217 consequent development of damage in compression even if no softening is

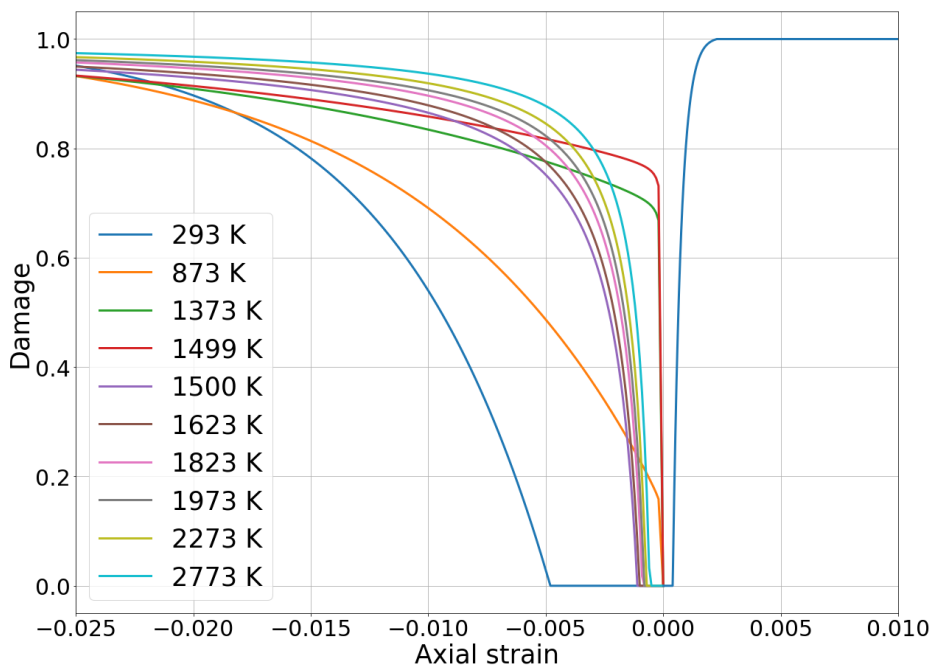


Figure 5: Damage-strain curves evolution with temperature as obtained from the  $\mu$ -model. The traction behavior is independent of temperature.

218 obtained in the stress-strain curves. Figure 5 presents the damage evolution  
 219 during the uniaxial compression and traction simulations of Figure 4. As can  
 220 be seen, even at temperatures above 1500 K where the behavior is ductile,  
 221 significant damage occurs with values of 0.8 or higher being reached even  
 222 at a relatively low strain level. This choice is related to the pronounced  
 223 grain boundary cracking that was observed in Salvo's tested samples at high  
 224 temperature [16].

## 225 4. Thermo-mechanical simulations of the laser heating tests

### 226 4.1. Mesh, boundary conditions and material properties

227 The simulations presented in the sequel have been performed with the  
 228 Finite Elements code Cast3M [28] developed by the CEA and used in the  
 229 fuel performance code ALCYONE [29]. A 2D axisymmetric representation  
 230 of a cross-section of the fuel disk is meshed. For the experiments with both  
 231 disk faces heated, half of the sample thickness is considered while the whole  
 232 thickness is considered for the experiments where only one face is heated.

233 Given the short duration of the laser heating experiments, thermal losses by  
234 radiative exchange, convection or possible losses related to the sample holder  
235 are not considered. The mesh of the fuel disk cross-section (half or quarter  
236 depending on the heating conditions) is illustrated in Figure 6 together with  
237 the thermal and mechanical boundary conditions. The mesh is especially  
238 refined below the laser heated surface (heat flux  $q_0$ ). The mesh density  
239 is then gradually increased with the distance from this zone. Mechanical  
240 displacements in the vertical direction at the bottom of the mesh are blocked.

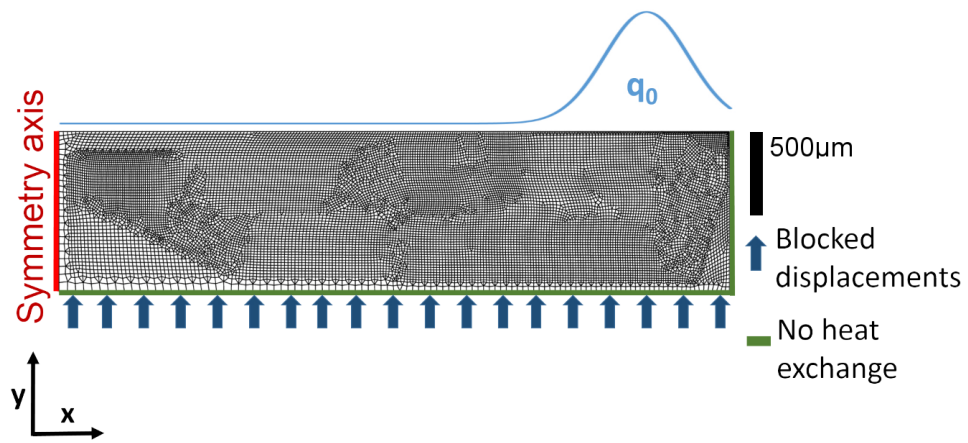


Figure 6: Mesh of the fuel pellet disk and thermo-mechanical boundary conditions considered

241 The fuel thermal and mechanical properties used in the simulations are  
 242 relative to non irradiated  $\text{UO}_2$  and extracted from the open literature [30,  
 243 31, 32]. The temperature dependent expressions are summarized in Table 2.

Property	Expression
Thermal conductivity (W.m <sup>-1</sup> .K <sup>-1</sup> ) [30]	$\lambda(T) = \frac{10^2}{7.5408 + 17.692t + 3.6142t^2 + \frac{6400}{t^{5/2}} \exp\left(\frac{-16.35}{t}\right)}$ with $t = T/1000$
Heat Capacity (J.mol <sup>-1</sup> .K <sup>-1</sup> ) [30]	298.15 K $\leq T \leq$ 3120 K: $C_p(T) = 52.1743 + 87.951t - 84.2411t^2 + 31.542t^3 - 2.6334t^4 - 0.71391t^{-2}$ with $t = T/100$
Density (kg/m <sup>3</sup> ) [30]	$\rho(T) = \rho_{273} \left( \frac{L(T)}{L_{273}} \right)^3$ with $\rho_{273} = 10963$ kg/m <sup>3</sup> , the density at 273 K
Thermal expansion coefficient (K <sup>-1</sup> ) [30] from [33]	$\alpha = \frac{1}{L} \left( \frac{dL}{dT} \right)$ 273 K $\leq T \leq$ 923 K: $L(T) = L_{273} (9.9734 \times 10^{-1} + 9.802 \times 10^{-6}T - 2.705 \times 10^{-10}T^2 + 4.391 \times 10^{-13}T^3)$ 923 K $< T \leq$ 3120 K: $L(T) = L_{273} (9.9672 \times 10^{-1} + 1.179 \times 10^{-5}T - 2.429 \times 10^{-9}T^2 + 1.219 \times 10^{-12}T^3 K^{-1})$
Young Modulus (GPa) [34]	$E(T) = (1 - 2.5p)(2.2710^2 - 1.54 \times 10^{-2}T - 9.60 \times 10^{-9}T^2)$
Poisson Ratio	0.3

with T the temperature in K and p the porosity

Table 2: UO<sub>2</sub> thermophysical and elastic properties used in the simulations

244 *4.2. Thermal loading and simulation*

245 In the considered axisymmetric configuration, the laser heat flux  $q_0$  (in  
246  $\text{W}/\text{m}^2$ ) represented in Figure 6 can be expressed as follows:

$$q_0(r, t) = (1 - X) \cdot f(t) \cdot I(r, \omega_{an}, R_{an}, P) \quad (10)$$

247 It is thus defined by the following terms:

- 248 • a time function  $f(t)$  indicating whether the laser power is on or off(1  
249 or 0) ,
- 250 • the intensity distribution  $I$ , in ( $\text{W}/\text{m}^2$ ), which is a function of  $r$  the  
251 radial position and of the characteristics of the annular beam (i.e.,  
252 beam waist  $\omega_{an}$ , radius  $R_{an}$  and power  $P$ ),
- 253 • a coefficient accounting for the losses along the optical path ( $1 - X$ ),  
254  $X$  being the sum of the losses along the optical path, including the  
255 reflectivity of the sample and of the sapphire window.

256 The intensity distribution of the annular gaussian beam  $I$  (in  $\text{W}/\text{m}^2$ ) is  
257 given by the following expression:

$$I(r, R_{an}, \omega_{an}) = I_{max} \exp \left[ -\frac{2(r - R_{an})^2}{\omega_{an}^2} \right] \quad (11)$$

258 with  $I_{max}$  ( $\text{W}/\text{m}^2$ ) the peak intensity of the Gaussian distribution:

$$I_{max} = \frac{P}{\pi \left( \frac{\omega_{an}^2}{2} \exp \left[ -\frac{2R_{an}^2}{\omega_{an}^2} \right] \right) + R_{an} \frac{\omega_{an} \sqrt{\pi}}{\sqrt{2}} \operatorname{erfc} \left( -\frac{\sqrt{2} \cdot R_{an}}{\omega_{an}} \right)} \quad (12)$$

259 where  $\operatorname{erfc}$  is the complementary error function and  $P$  the laser power  
260 given in W.

261 To check the thermal modeling of the laser heating test, the first test series  
262 has been simulated. The initial uniform temperature of the disk equals 1123  
263 K ( $850^\circ\text{C}$ ). The heat flux  $q_0$  resulting from the laser beams on each side of the  
264 disk ( $P = 620 \text{ W}$ ,  $R_{an} = 3.5 \text{ mm}$  and  $\omega_{an} = 0.5 \text{ mm}$ ) is then prescribed during  
265 20 ms. The calculated radial temperature profiles at the disk surface are then  
266 plotted every 5 ms, as shown in Figure 7. A good agreement between the

267 calculated radial profiles of temperature and the measurements during the  
 268 experiments by infrared imaging is obtained. In particular, the calculated  
 269 peak temperature is close to the measured one. Moreover, these results are  
 270 in agreement with the temperature profiles calculated with the COMSOL  
 271 solver used by Vidal et al. to design these laser heating tests [12].

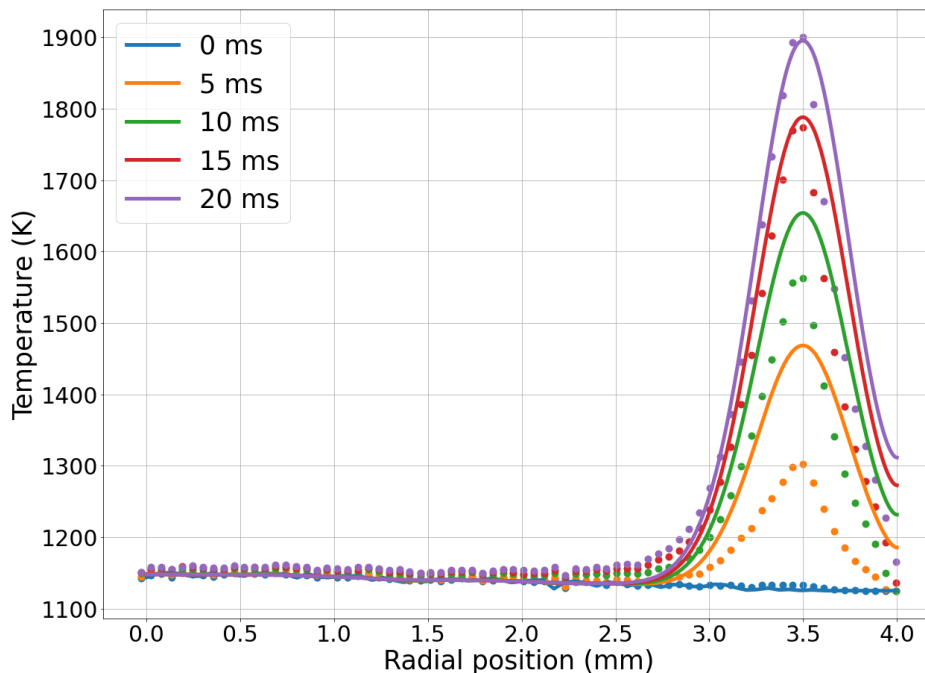


Figure 7: Simulated (continuous lines) and measured (dots) surface temperatures during a 20 ms duration and 620 W laser heating experiment

272 Simulations accounting for radiative heat exchanges between the sample  
 273 and the sapphire windows have been done using values of the total hemi-  
 274 spherical emissivity available in the literature for both  $UO_2$  and sapphire  
 275 [32, 35]. Radiative heat exchanges had a negligible impact on the calculated  
 276 temperatures. These results confirmed that they can be neglected in the  
 277 simulations.

#### 278 4.3. Thermo-elastic simulation

279 The second test series of laser heating experiments is now considered.  
 280 Thermo-elastic simulations are first performed. The initial temperature of  
 281 the sample is in this case the room temperature. The calculated peak surface

282 temperature reaches 973 K (700°C) during the 100 ms - 150 W test and 2273  
 283 K (2000°C) during the 100 ms - 300 W test, as shown in Figure 8. Heating  
 284 takes place only on one of the disk face. No temperature measurement is  
 285 available.

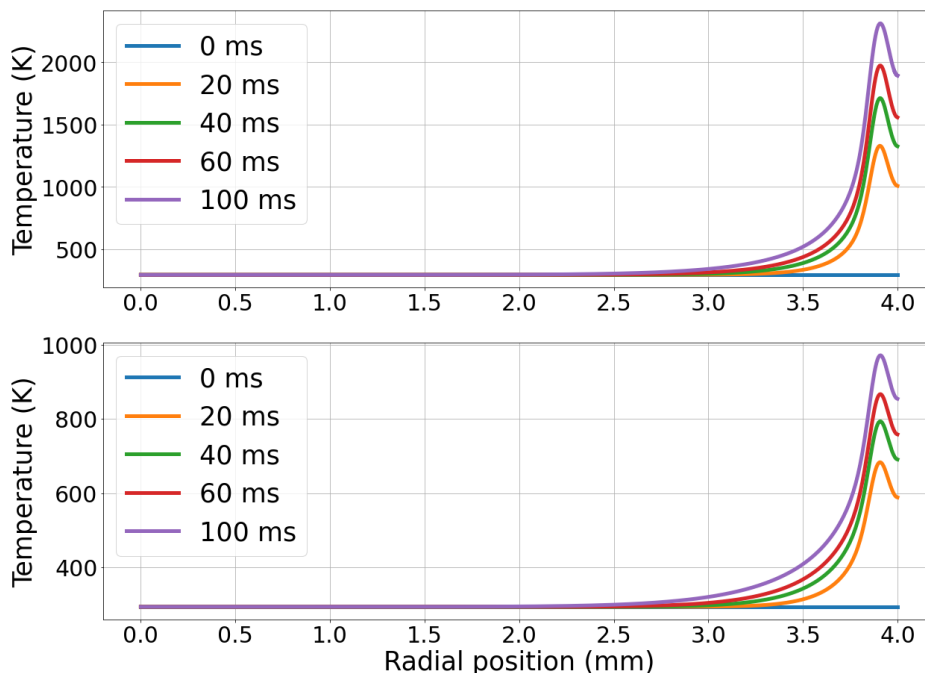


Figure 8: Calculated evolution of the surface temperature during the 100 ms - 300 W (top) and 100 ms - 150 W (bottom) experiments

286 The calculated strain rates show that these experiments are relevant for  
 287 the study of RIA transient mechanisms since the strain rates in the heated  
 288 zone reach more than 3 /s during the 100 ms - 300 W experiment. The  
 289 calculated radial profiles of the radial, hoop and axial stresses on the heated  
 290 surface (peak laser power) during this test are plotted in Figure 9.

291 Significant compressive peaks are obtained for the two first stress com-  
 292 ponents near the pellet periphery. The stress values are however unrealistic.  
 293 The maximum hoop stress reaches -6000 MPa. As detailed in part 3, the com-  
 294 pressive strength of  $\text{UO}_2$  at room temperature does not exceed 1000 MPa.  
 295 Looking now at the radial stress distribution in the disk presented in Figure  
 296 10, one may note that a strong radial compression state holds in the heated  
 297 region of the sample (circled in Figure 10) and a concomitant radial tensile

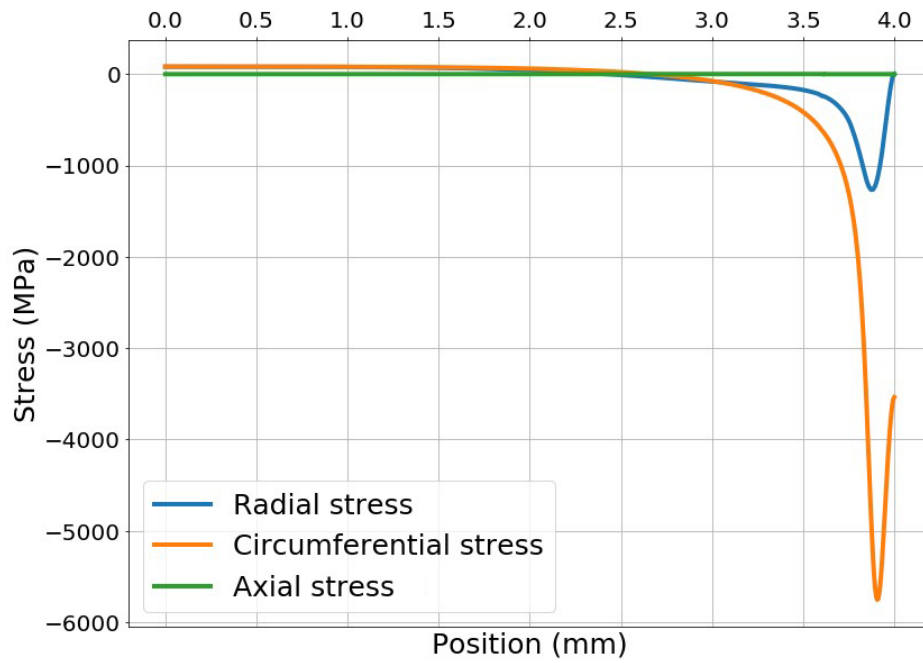


Figure 9: Thermo-elastic radial, hoop and axial stresses radial profiles at the heated surface of the disk after 100 ms of annular laser heating at 300 W.

298 state is observed in the area beneath it.

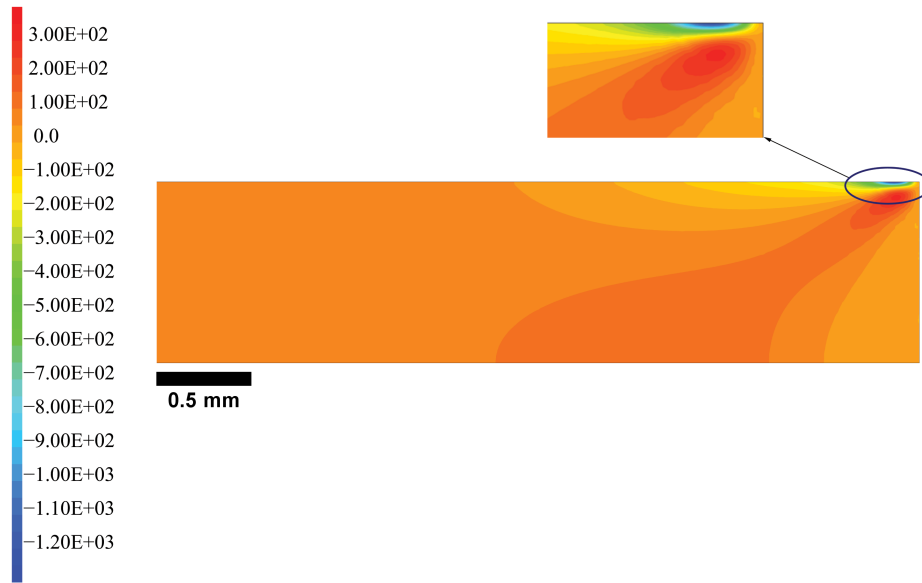


Figure 10: Calculated radial stress distribution (in MPa) within the fuel disk after 100 ms of annular laser heating at 300 W on the top surface

299 The magnitude of these tensile radial stresses depends on the first order of  
 300 the compressive stresses in the heated region of the disk. Radial stresses being  
 301 the driving force behind circumferential cracking, it is of utmost importance  
 302 to precisely model the behavior of  $\text{UO}_2$  in compression and during fast tem-  
 303 perature rise if one wants to assess the fragmentation of the fuel during the  
 304 laser heating experiments. With the high thermo-elastic compressive stresses  
 305 reached in the heated zone, the calculated tensile stresses in the region (al-  
 306 most 250 MPa) beneath exceed the  $\text{UO}_2$  tensile strength. Circumferential  
 307 cracking of the sample during the heating phase is thus expected.

#### 308 4.4. Thermo-mechanical analysis with the $\mu$ -model

309 The  $\mu$ -model was then used for the simulation of the two 100 ms ex-  
 310 periments of the second test series. During the simulation of the 150 W  
 311 experiment, damage develops only in the heated area. The damage level  
 312 reached is moderate with a maximum close to 0.5. As expected, this damage  
 313 is the consequence of the high compressive stresses reached in the heated  
 314 area, as shown by the isovalues of  $Y_c$  given in Figure 11. Values of  $Y_t$  during  
 315 this experiment remain below  $10^{-4}$ . Crushing is thus the damage mode that  
 316 take place in the laser heated area.

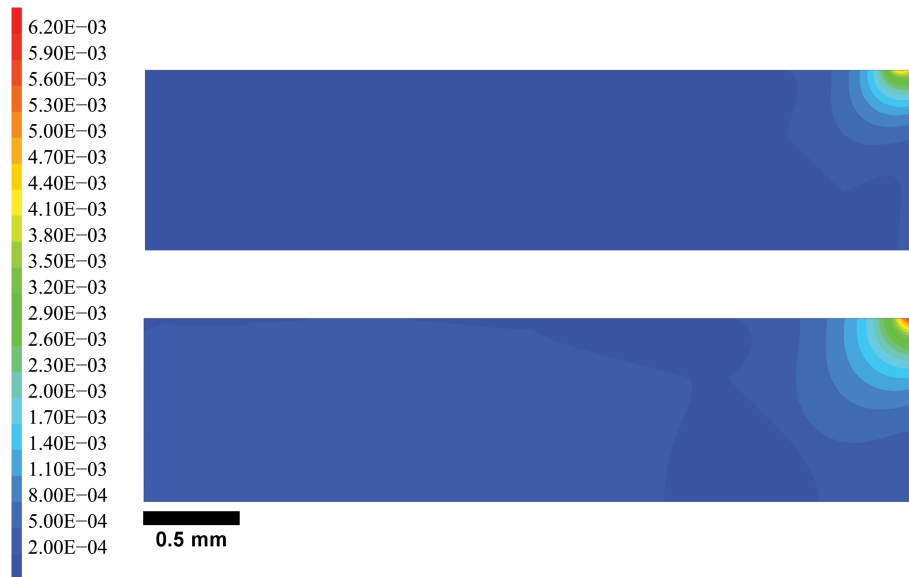


Figure 11: Calculated  $Y_c$  values at 40 (top) and 100 ms (bottom) during the simulation of the 150 W - 100 ms experiment

317 During the simulation of the 300 W experiment, two distinct damage  
318 zones are observed before the failure of the sample (at 40 and 45 ms), as  
319 shown in Figure 12.

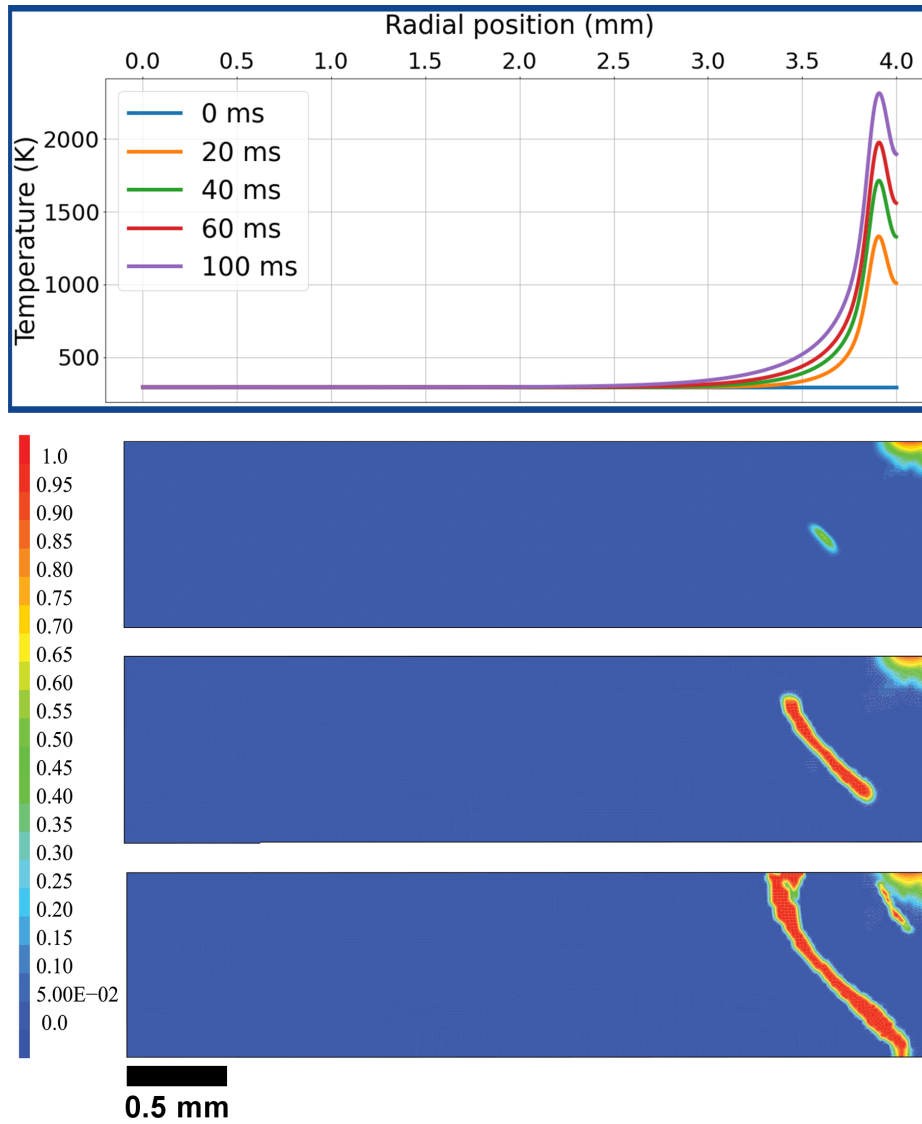


Figure 12: Calculated damage values at 40, 43 and 46 ms during the simulation of the 100 ms - 300 W experiment. Top graph: calculated radial temperature profiles at various times

320 As for the simulation of the 150 W test, the area directly heated by  
 321 the laser is damaged by crushing (local compression). The area beneath the  
 322 heated zone is on the contrary damaged by the development of tensile stresses  
 323 that exceed the material strength (cracking). This is confirmed by the iso-  
 324 values of  $Y_t$ , plotted in Figure 13 at different times during the experiment.

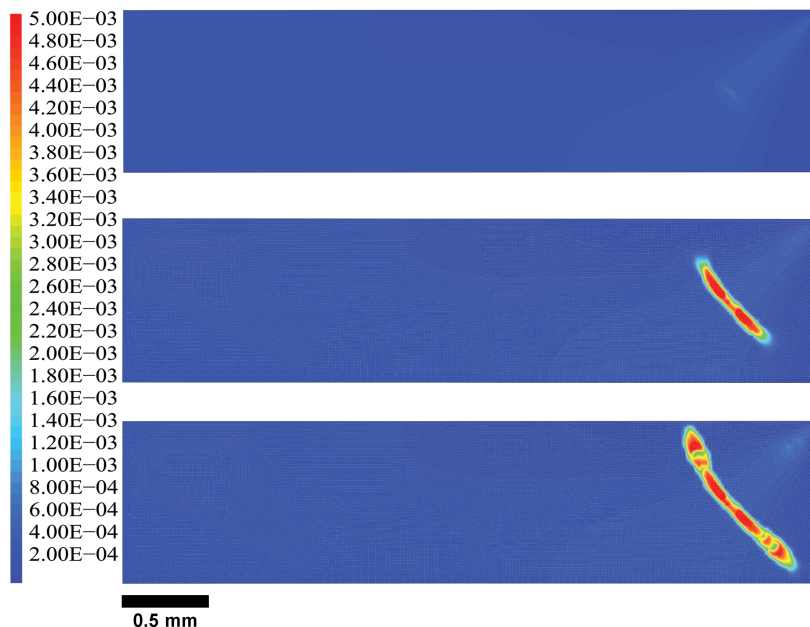


Figure 13: Calculated  $Y_t$  values at 40, 43 and 45 ms during the 300 W - 100 ms experiment. The maximum reached at 45ms is  $8E-03$ .

325 At 39-40 ms,  $Y_t$  starts to increase beneath the heated area where the  
 326  $Y_c$  variable is dominant (slight increase visible on Figure 13). This simula-  
 327 tion result is consistent with the radial stress distribution calculated in the  
 328 thermo-elastic simulation of the test, see Figure 10. In consequence of the  
 329 high tensile radial stresses reached beneath the heated area, a circumferential  
 330 fracture develops as can be seen in Figure 12. A good agreement between  
 331 the calculated (46 ms) and recorded circumferential cracking time ( $\sim 40$  ms)  
 332 of the disk is obtained, showing the good capability of the model to correctly  
 333 assess the compressive stresses in the heated zone and the tensile counter-  
 334 part. The post-mortem SEM examination of the sample shown in Figure 14  
 335 confirmed the development of a circumferential crack near the pellet periph-

336 ery and the micro-damage of the material in the heated area that had led to  
337 some visible grain boundary cracking.

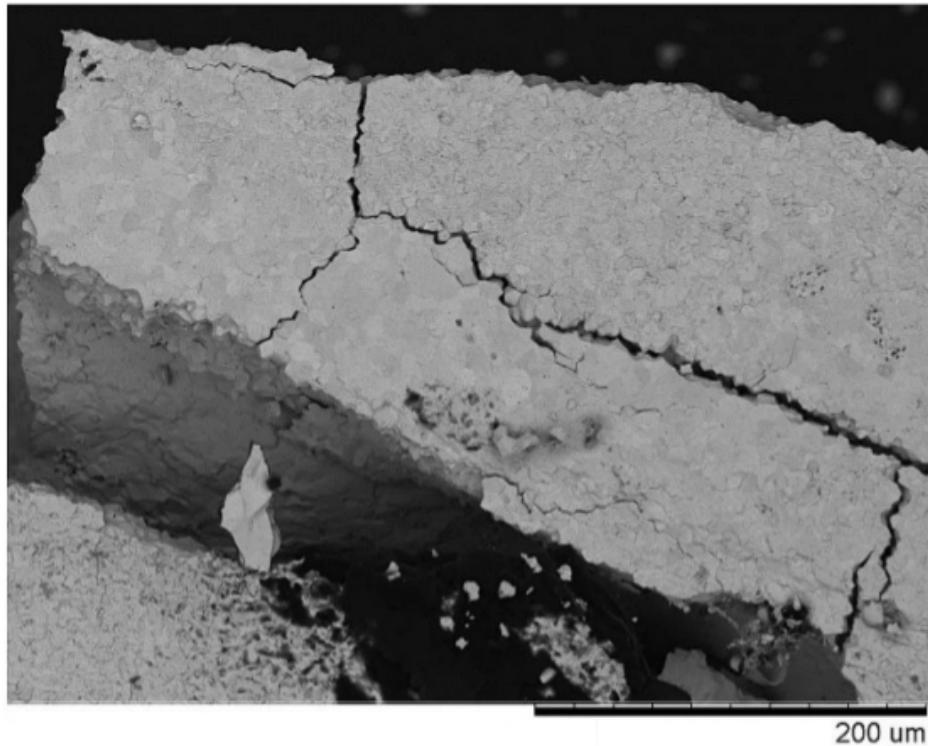


Figure 14: SEM examination of the  $\text{UO}_2$  disk periphery after the 300 W - 100 ms experiment

## 338 5. Discussion

339 Thermo-mechanical simulations of the behavior of  $\text{UO}_2$  samples submit-  
340 ted to high-power laser heating have been presented in this paper. In a first  
341 part, the relevance of the thermal and mechanical models are discussed. In  
342 a second part, the applicability of the proposed laser heating technique to  
343 irradiated nuclear fuel and fission gas release studies during RIA simulated  
344 thermal transients is discussed.

### 345 5.1. Relevance of the thermal and mechanical models

346 The radial temperature profile and peak temperature are well reproduced  
347 by the thermal model implemented in this work even if the thermal bound-

348 aries conditions do not account for heat exchange with the surrounding ma-  
349 terials. The shape of the radial temperature profile is however not perfectly  
350 reproduced since the calculated profile is slightly wider than the experimental  
351 one.

352 This fact may come from a discrepancy between the theoretical intensity  
353 distribution of an annular gaussian beam (Eq.11) and the one obtained in our  
354 setup. It is therefore also possible to use the experimental intensity profile of  
355 the laser (see insert on Figure 2) instead of the theoritcal one. Such profile  
356 measurements were not available for the presentend experiments.

357 A discrepancy between the measured and calculated temperatures dur-  
358 ing the first few milliseconds of the experiment can also be observed. It is  
359 supposed to be induced by the temporal incertitude of the measurements.  
360 The laser pulse and thermal camera were not synchronized and with an ac-  
361 quisition rate of 5 ms, the incertitude can then be as high as 5 ms. In future  
362 work, the laser pulse and thermal camera will be synchronized.

363 The proposed mechanical model is able to reproduce the mechanical be-  
364 havior, damage and fracture mechanisms of uranium dioxide submitted to  
365 laser-heating experiments (crushing and cracking with stress relaxation). As  
366 shown in this paper, the craking time experimentally recorded is well repro-  
367 duced with this model provided the model parameters for both tension and  
368 compression are well defined from material tests performed at high strain  
369 rates and temperatures. While the incertitude from the visible camera rate  
370 of acquisition of 800 images/s is inferior to 1.25 ms, one could argue that the  
371 definition of the instant of cracking from highly saturated images such as the  
372 ones swhowed in Figure 15 is arbitrary. As can be seen in Figure 15 from the  
373 thermal radiation recorded by the camera during the test, it is however sure  
374 that cracking occurred between 36 and 45 ms. A conservative assessment  
375 then leads to choose 40 ms as the time where the sample begins to lose its  
376 integrity.

377 To lift uncertainties regarding the beginning of cracking, other measur-  
378 ing devices less prone to saturation could be used by using an optical device  
379 filtering thermal radiation. Future works will then aim to further validate  
380 the cracking criterion with a better determination of the time and visuali-  
381 sation of the cracking. While it is true that the definition of the beginning  
382 of cracking from the showed image sequence will highly depend on the cho-  
383 sen criterion, it is interesting to point out that this instrumentation clearly  
384 showed that cracking happened during the heating phase and not during the  
385 cooling phase. Cracks and fragments indicated by blue arrows in Figure 15

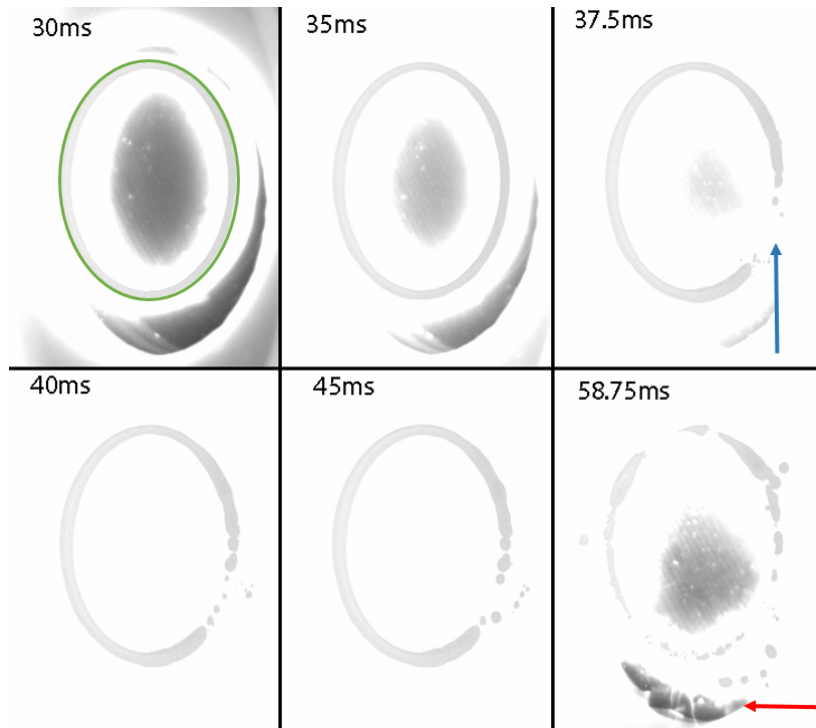


Figure 15: Evolution of the thermal radiation recorded by a high-speed visible camera during the 100 ms - 300 W experiment. The green circle roughly indicate the periphery of the sample. Sample's radius is 4mm. The blue arrow point out the beginning of the fracturation. The red arrow indicate visible fragments seen during the experiment.

386 are in fact clearly visible after 50 ms. In thermal loading sequences, one  
 387 usually expects significant damage to take place during the cooling phase  
 388 rather than during the heating phase. The occurrence of damage during the  
 389 heating phase could not have been detected without a proper instrumenta-  
 390 tion. It shows the importance to perform out-of-pile experiments at the lab  
 391 scale with sophisticated instrumentation, such instrumentation being easier  
 392 to implement than in research reactors.

### 393 5.2. Applicability to irradiated nuclear fuel

394 From the analysis of the stress state in the sample during the laster exper-  
 395 iments, it is clear that the area of the sample directly heated is subjected to  
 396 high compressive stresses. This compression state and its tensile counterpart  
 397 can lead to damage of the microstructure of the material by local crush-  
 398 ing/cracking potentially weakening the grain boundaries. If pre-irradiated

399 samples were to be tested under the same loading sequence, one could ex-  
400 pect fission gas release related to grain boundary cracking to take place,  
401 by the same mechanism than during RIA transients. The ability to induce  
402 grain boundary cracking in the periphery of the sample subjected to a biaxial  
403 stress state, as confirmed by SEM examination, is particularly interesting.  
404 Indeed, in high burnup fuels, the fragmentation of the pellet rim is a well-  
405 known phenomenon piloting fission gas release during RIA transients [9]. As  
406 such, having the capacity to reproduce RIA thermal conditions and induc-  
407 ing equivalent stress states in some parts of the fuel sample within a heavily  
408 instrumented environment could allow precise investigations regarding this  
409 topic. In this respect, it should also be possible to uncouple compression and  
410 tensile induced damage (i.e., inducing compression damage without tensile  
411 related damage) with this technique and thus to quantify the contribution  
412 of each phenomenon to fission gas release. This could potentially give great  
413 insights on fission gas release kinetics. In fact, during the power increasing  
414 phase of a RIA, the fuel periphery is first subjected to compressive stresses.  
415 Whether fission gas release takes place during this period or not is of impor-  
416 tance to assess the potential for clad ballooning and burst if the fission gas  
417 related pressure reached inside the rod is too high. The transients showed  
418 in this paper do not reproduce a full RIA thermal sequence departing from  
419 normal operating conditions where a radial parabolic temperature gradient  
420 holds. Future works will aim to tend towards a more representative thermal  
421 loading sequence. The use of a second Gaussian beam to reproduce both  
422 the dynamic increase of temperature in the inner part of the sample and the  
423 parabolic shape of the temperature profile during the cooling phase of the  
424 transient is currently under study. The dynamic adjustment of the power  
425 of this secondary beam should also allow a controlled cooling in order to  
426 reproduce the whole RIA thermal transient.

## 427 **6. Conclusion**

428 In this paper, a thermo-mechanical model suitable for the interpretation  
429 of laser heating experiments simulating the power increasing phase of a RIA  
430 transient has been detailed. The specificity of the experiments lies in the  
431 annular heating of the  $\text{UO}_2$  disk samples that is intended to reproduce the  
432 peaked temperature radial profile in the pellet during this type of transient.  
433 The thermal model includes a description of the heat deposition on the pel-  
434 let surface and of the heat transfer within the thickness and radius of the

435 UO<sub>2</sub> disk. The mechanical modeling relies on an adaptation of the damage  
436  $\mu$ -model proposed by Mazars et al. [19] for concrete materials to uranium  
437 dioxide. It describes cracking and crushing of the material depending on the  
438 loading mode (tension or compression dominated) and on temperature. The  
439 brittle - ductile transition in compression is in particular well reproduced.  
440 The parameters fitting is based on available uniaxial compression tests per-  
441 formed at high strain rates and on bending tests performed at moderate  
442 strain rates. The application of the mechanical model to the annular laser  
443 heating experiments led to a good estimation of the crushing and cracking  
444 location (near the pellet periphery), of the crack orientation (circumferential)  
445 and of the beginning of cracking. More experiments with on-line tempera-  
446 ture measurements and image recording are however needed to better assess  
447 the tensile cracking kinetics and the loading conditions leading to crushing.  
448 The SEM analysis performed post-mortem showed the development of grain  
449 boundary cracking in the heated zone. These annular laser heating experi-  
450 ments could therefore be used to study fission gas release mechanisms during  
451 lab simulated RIA transients.

452 **References**

- 453 [1] I. Guénot-Delahaie, J. Sercombe, T. Helfer, P. Goldbronn, Fédérici,  
454 T. Le Jolu, A. Parrot, C. Delafoy, C. Bernaudat, Simulation of  
455 reactivity-initiated accident transients on  $\text{UO}_2$ -M5<sup>®</sup> fuel rods with AL-  
456 CYONE V1.4 fuel performance code, Nuclear Engineering and Technol-  
457 ogy 50 (2018) 268–279.
- 458 [2] J. Sercombe, I. Aubrun, C. Nonon, Power ramped cladding stresses and  
459 strains in 3D simulations with burnup-dependent pellet–clad friction,  
460 Nuclear Engineering and Design 242 (2012) 164–181.
- 461 [3] J. Sercombe, T. Helfer, E. Federici, D. Leboulch, T. Le Jolu, A. Hel-  
462 louin de Ménibus, C. Bernaudat, 2D simulation of hydride blister crack-  
463 ing during a RIA transient with the fuel code ALCYONE, EPJ Nuclear  
464 Sciences & Technologies 2 (2016) 22.
- 465 [4] A. Moal, V. Georgenthum, O. Marchand, SCANAIR: A transient fuel  
466 performance code Part One: General modelling description, Nuclear  
467 Engineering and Design 280 (2014) 150–171.
- 468 [5] V. Georgenthum, A. Moal, O. Marchand, SCANAIR a transient fuel  
469 performance code Part two: Assessment of modelling capabilities, Nu-  
470 clear Engineering and Design 280 (2014) 172–180.
- 471 [6] P. M. M.E. Cuningham, C.E. Beyer, G. Berna, FRAPTRAN: A Com-  
472 puter Code for the Transient Analysis of Oxide Fuel Rods, Technical  
473 Report NUREG/CR-6739 - VOL.1, U.S Nuclear Regulatory Commis-  
474 sion, 2001.
- 475 [7] M. Suzuki, T. Fuketa, H. Saitou, Analysis of Pellet-Clad Mechanical  
476 Interaction Process of High-Burnup PWR Fuel Rods by RANNS Code  
477 in Reactivity-Initiated Accident Conditions, Nuclear Technology 155  
478 (2006) 282–292.
- 479 [8] W. Lyon, R. Montgomery, N. Jahingir, S. Yagnik, Capabilities of the  
480 FALCON Steady State and Transient Fuel Performance Code, in: Pro-  
481 ceedings of the 2004 International Meeting on LWR Fuel Performance.
- 482 [9] J. Papin, B. Cazalis, J. M. Frizonnet, J. Desquines, F. Lemoine, V. Geor-  
483 genthum, F. Lamare, M. Petit, Summary and Interpretation of the  
484 CABRI REP-Na Program, Nuclear Technology 157 (2007) 230–250.

- 485 [10] T. Fuketa, T. Sugiyama, F. Nagase, Behavior of 60 to 78MWd/kgU  
486 PWR Fuels under Reactivity-Initiated Accident Conditions, Journal of  
487 Nuclear Science and Technology 43 (2006) 1080–1088.
- 488 [11] Nuclear Fuel Behaviour Under Reactivity-initiated Accident  
489 (RIA) Conditions - State-of-the-art Report, Technical Report,  
490 NEA/CSNI/R(2010)1, 2010.
- 491 [12] T. Vidal, L. Gallais, J. Faucheux, H. Capdevila, J. Sercombe, Y. Pon-  
492 tillon, Simulation of reactivity initiated accident thermal transients on  
493 nuclear fuels with laser remote heating, Journal of Nuclear Materials  
494 530 (2020) 151944.
- 495 [13] P. Ruello, K. Becker, K. Ullrich, L. Desgranges, C. Petot, G. Petot-  
496 Ervas, Thermal variation of the optical absorption of  $\text{UO}_2$ : determina-  
497 tion of the small polaron self-energy, Journal of Nuclear Materials 328  
498 (2004) 46–54.
- 499 [14] K. W. M. Bober, J. Singer, Spectral Reflectivity and Emissivity Mea-  
500 surements of Solid and Liquid  $\text{UO}_2$  at 458, 514.5 and 647 nm as a Func-  
501 tion of Polarization and Angle of Incidence, Technical Report, Kern-  
502 forschungszentrum Karlsruhe - Institut für Neutronenphysik und Reak-  
503 tortechnik, 1980.
- 504 [15] M. Salvo, J. Sercombe, T. Helfer, P. Sornay, T. Désoyer, Experimental  
505 characterization and modeling of  $\text{UO}_2$  grain boundary cracking at high  
506 temperatures and high strain rates, Journal of Nuclear Materials 460  
507 (2015) 184–199.
- 508 [16] M. Salvo, J. Sercombe, J.-C. Ménard, J. Julien, T. Helfer, T. Désoyer,  
509 Experimental characterization and modelling of  $\text{UO}_2$  behavior at high  
510 temperatures and high strain rates, Journal of Nuclear Materials 456  
511 (2015) 54–67.
- 512 [17] R. F. Canon, J. T. A. Roberts, R. J. Beals, Deformation of  $\text{UO}_2$  at High  
513 Temperatures, Journal of The American Ceramic Society 54 (1971) 105–  
514 112.
- 515 [18] A. G. Evans, R. W. Davidge, The strength and fracture of stoichiometric  
516 polycrystalline  $\text{UO}_2$ , Journal of Nuclear Materials 33 (1969) 249–260.

- 517 [19] J. Mazars, F. Hamon, S. Grange, A new 3D damage model for concrete  
518 under monotonic, cyclic and dynamic loadings, *Materials and Structures*  
519 48 (2015) 3779–3793.
- 520 [20] J. Mazars, A description of micro- and macroscale damage of concrete  
521 structures, *Engineering Fracture Mechanics* 25 (1986) 729–739.
- 522 [21] B. Michel, J. Sercombe, G. Thouvenin, R. Chatelet, 3D fuel cracking  
523 modelling in pellet cladding mechanical interaction, *Engineering Frac-*  
524 *ture Mechanics* 75 (2008) 3581–3598.
- 525 [22] T. Helfer, Castelier, P. Garcia, Two dimensional modelling of PWR  
526 fuel rods - analysis of fuel cracking, in: *Euromech - Mecamat 2006 :*  
527 *9th European Mechanics of Materials Conference - Local Approach to*  
528 *Fracture*.
- 529 [23] J. Byron, Yield and flow of polycrystalline uranium dioxide, *Journal of*  
530 *Nuclear Materials* 27 (1968) 48–53.
- 531 [24] Y. Guerin, Etude par compression a hautes temperatures de la deforma-  
532 tion plastique du bioxyde d’uranium polycristallin, *Journal of Nuclear*  
533 *Materials* 56 (1975) 61–75.
- 534 [25] T. Helfer, B. Michel, J.-M. Proix, M. Salvo, J. Sercombe, M. Casella,  
535 Introducing the open-source mfront code generator: Application to me-  
536 chanical behaviours and material knowledge management within the  
537 PLEIADES fuel element modelling platform, *Computers & Mathematics*  
538 *with Applications* 70 (2015) 994–1023.
- 539 [26] N. Igata, K. Domoto, Fracture stress and elastic modulus of uranium  
540 dioxide including excess oxygen, *Journal of Nuclear Materials* 45 (1973)  
541 317–322.
- 542 [27] F. Sauter, S. Leclercq, Modeling of the non-monotonous viscoplastic  
543 behavior of uranium dioxide, *Journal of Nuclear Materials* 322 (2003)  
544 1–14.
- 545 [28] Cast3m 2019, <http://www-cast3m.cea.fr/>, 2019.
- 546 [29] B. Michel, C. Nonon, J. Sercombe, F. Michel, V. Marelle, Simulation of  
547 pellet-cladding interaction with the PLEIADES fuel performance soft-  
548 ware environment, *Nuclear Technology* 182 (2013) 124–137.

- 549 [30] J.K. Fink, Thermophysical properties of uranium dioxide, Journal of  
550 Nuclear Materials 279 (1999) 1–18.
- 551 [31] Hagrman, D T, Allison, C M, Berna, G A, SCDAP/RELAP5/MOD 3.1  
552 code manual: MATPRO, A library of materials properties for Light-  
553 Water-Reactor accident analysis, 1995.
- 554 [32] I. A. E. Agency, Thermophysical properties database of materials for  
555 light water reactors and heavy water reactors: final report of a co-  
556 ordinated research project, 1999-2005., International Atomic Energy  
557 Agency, 2006.
- 558 [33] D. Martin, The thermal expansion of solid  $\text{UO}_2$  and (U, Pu) mixed  
559 oxides - A review and recommendations, Journal of Nuclear Materials  
560 152 (1988) 94–101.
- 561 [34] D. Martin, The elastic constants of polycrystalline  $\text{UO}_2$  and (U, Pu)  
562 mixed oxides : A review and recommendations, High Temperatures.  
563 High Pressures 21.1 (1989) 13–24.
- 564 [35] A. M. Wittenberg, Total Hemispherical Emissivity of Sapphire, Journal  
565 of the Optical Society of America 55 (1965) 432.